Metallurgical and Materials Data 4, no. 1 (2026): 1-6

Publisher: Association of Metallurgical Engineers of Serbia

Metallurgical and Materials Data

www.metall-mater-data.com

Molecular dynamics simulation of physical and mechanical properties of CrCoFeNiMn high-entropy alloy

Rajdeep Saha[1,3]*, Sudipta Chell[2,3]*

[1]Department of Metallurgical and Materials Engineering, Indian Institute of Technology Kharagpur, Kharagpur, India
[2]Reliance Industries Limited, Jamnagar, India
[3]Department of Metallurgical and Materials Engineering, National Institute of Technology Durgapur, Durgapur, India

ARTICLE INFORMATION:

https://doi.org/10.56801/MMD89

Received 23 May 2026
Accepted 8 October 2026
Type of paper: Research paper

ORCID iDs:
R.S. https://orcid.org/0009-0006-4820-838
S.C. https://orcid.org/0009-0005-8984-0843

Copyright: © 2026 by the authors, under the terms and conditions of the Creative Commons Attribution (CC BY) license (https://creativecom-mons.org/licenses/by/4.0/).

ABSTRACT

The Cantor alloy (equiatomic CrCoFeMnNi high-entropy alloy) is a promising structural material because of its strength–ductility combination, although its five-element composition makes some properties difficult to be characterized experimentally. This study uses molecular dynamics simulations in LAMMPS with the 2NN MEAM potential to evaluate the melting point, specific heat capacity at constant volume, heat of fusion, hardness, and Young's modulus. The calculated melting point is 1547 K, consistent with reported values. The specific heat capacity at constant volume and heat of fusion are 454.15 J/(kg·K) and 21.75 kJ/kg, respectively. Simulated spherical nanoindentation gives a hardness of 7.58 GPa and a Young's modulus of 173.3 GPa. The hardness exceeds experimental values and is therefore interpreted as an idealized upper-bound estimate for the defect-free, high-strain-rate model. Overall, the simulations provide internally consistent thermophysical and mechanical estimates for the Cantor alloy, while experimental validation remains necessary for application-level conclusions.

Keywords: high-entropy alloy; Cantor alloy; molecular dynamics; modelling; LAMMPS

1. Introduction

High-entropy alloys (HEAs) are composed of five or more principal elements in near-equiatomic proportions. This compositional concept can produce property combinations that are attractive for structural applications (Cantor et al. 2004; Caramarin et al. 2024; Zhangwei Wang et al. 2019; Kauffmann et al. 2017). The equiatomic CrCoFeMnNi HEA, commonly known as the Cantor alloy, contains chromium, cobalt iron, manganese, and nickel in equal proportions and forms a stable face-centered cubic (FCC) structure with a large number of slip systems (Özgün et al. 2022; Yue et al. 2022; Kim et al. 2020). It has been reported to exhibit good high-temperature structural stability (Gali and George 2013; Pei et al. 2023; Wei et al. 2022) and an excellent strength–ductility balance, particularly at cryogenic temperatures (Sun et al. 2018; Zeng et al. 2021). These properties make the alloy relevant to demanding structural environments, including potential nuclear and aerospace applications (Otto et al. 2013; Choi et al. 2018).

The five-element composition of the Cantor alloy makes comprehensive experimental characterization challenging. Although macroscopic properties such as hardness and thermal conductivity can be measured experimentally, the atomistic interactions underlying these properties are more difficult to be resolved rectly. Molecular dynamics (MD) simulations provide a complementary approach by modelling atomic motion and response under controlled conditions. Previous studies have examined the structural and mechanical behaviour of HEAs, but individual thermophysical and mechanical properties are often treated separately. The present study therefore evaluates several properties within a single atomistic model.

The melting point is an important thermophysical parameter for assessing the high-temperature behaviour of the alloy. Previous studies have reported melting temperatures in the range of 1500–1600 K (Cantor et al. 2004; Liu et al. 2023), while an atomistic two-phase coexistence study using a machine-learned interatomic potential obtained a value in close agreement with experiment (Balyakin and Rempel 2022). The present work estimates the melting point of the Cantor alloy and also evaluates its specific heat capacity at constant volume and heat of fusion. Together, these quantities characterize the simulated system's thermal response and energy changes associated with heating and melting.

Hardness and Young's modulus characterize resistance to localized plastic deformation and elastic deformation, respectively. Experimental nanoindentation studies report hardness values of approximately 2–3 GPa and a Young's modulus near 200 GPa at room temperature (Gludovatz et al. 2014), while experimental and computational studies report Young's modulus values of approximately 160–210 GPa depending on microstructure, temperature, and loading conditions (Lohmuller et al. 2018; Maier-Kiener et al. 2017). Molecular dynamics studies have

* Corresponding authors.
E-mail address: raj.deep.29sep@gmail.com (Rajdeep Saha); sudiptachell89@gmail.com (Sudipta Chell)

also examined tensile and compressive loading of CrCoFeMnNi-based alloys (Gong et al. 2025; L. Zhang et al. 2021). Many such studies use EAM potentials; the MEAM formulation additionally includes angular contributions and therefore provides a useful alternative for describing multicomponent metallic systems (B.-J. Lee et al. 2010).

Reliable MD calculations require an appropriate interatomic potential, a sufficiently large simulation cell, adequate equilibration and production time, and, where feasible, averaging over independent configurations (Mahata et al. 2022).

scale Atomic/Molecular Massively Parallel Simulator (LAMMPS) with a second-nearest-neighbour modified embedded-atom method (2NN MEAM) potential. Unlike much of the previous MD literature on the Cantor alloy, which reports one or two properties in isolation, the present work evaluates the melting point, specific heat capacity at constant volume, heat of fusion, hardness, and Young's modulus within a single, internally consistent 2NN MEAM model. Table 1 compares the calculated values with selected literature data.

2. Simulation Model and Methods

Molecular dynamics simulations were performed using LAMMPS. Each simulation used an input script defining the atomic configuration, boundary conditions, ensemble, timestep, runtime, and output settings. The input script, together with the alloy's MEAM potential file, was then used by the compiled LAMMPS executable to perform the calculations and generate the simulation output.

The interatomic interactions were modelled using the second-nearest-neighbour modified embedded-atom (2NN MEAM) method (Mahata et al. 2022; B.-J. Lee et al. 2001), extended to the five-element Cr-Co-Fe-Mn-Ni system following the parameterization and validation approach of Choi et al. (2018). All simulations were performed using LAMMPS (Thompson et al. 2022). Before the production runs, the potential was checked against known equilibrium lattice constants and cohesive energies of the constituent metals. The MEAM potential files were obtained from the NIST Interatomic Potentials Repository.

2.1. Simulation for melting-point calculation

The LAMMPS 'metal' unit system and 'periodic' boundary conditions in all three dimensions were used to represent a bulk material without free-surface effects. An FCC lattice was generated in a cubic simulation box spanning 20 lattice units along each axis, corresponding to 32,000 atoms (20 × 20 × 20 unit cells × 4 atoms per FCC unit cell). Five atom types were defined, and an approximately equiatomic composition was generated by sequential random reassignment of atom types.

The system was first relaxed by conjugate-gradient energy minimization, using convergence criteria of 10^{-15} eV for energy and 10^{-15} eV/Å for force and a maximum of 10,000 iterations. Initial velocities were assigned from a Gaussian distribution at 300 K. The system was then equilibrated in the NVT ensemble at 300 K using a Nosé–Hoover thermostat with a damping parameter of 0.01 ps. The timestep was 0.001 ps, and simulation was performed or 100,000 timesteps (100 ps). After equilibration, the NVT fix was removed and the system was evolved in the NVE ensemble while energy was added at 1 eV/ps every 100 timesteps. Thermodynamic quantities were recorded every 10,000 timesteps and atomic configurations every 100,000 timesteps. The simulation was allowed to run up to 1,000,000,000 timesteps (1,000,000 ps); the melting transition was observed at timestep 10,250,000. The melting point was identified from the abrupt change in the thermodynamic response, supported by the corresponding structural change (Figures 1 and 2).

2.2. Simulation for nanoindentation

Nanoindentation simulations were performed to estimate the hardness and elastic modulus of the alloy (Liu et al. 2023; Alabd Alhafez et al. 2019). The model used 'periodic' boundary conditions in the x and y directions and a shrink-wrapped boundary in the z direction to provide a free surface for indentation. A cylindrical sample with a radius and height of 100 Å was generated, and a 10 Å-thick lower region was constrained to represent a rigid base. Energy minimization used the conjugate-gradient method with convergence criteria of 10^{-20} eV for energy and 10^{-20} eV/Å for force. The timestep was 0.001 ps.

The nanoindentation procedure comprised loading, holding, and unloading stages, all performed in the NVE ensemble. A spherical indenter with a radius of 30 Å was centered at (x, y) = (0, 0) and moved along the z axis. Spherical indentation provides a gradual elastic-plastic transition and permits analysis using Hertzian contact concepts and the Oliver-Pharr method (D.-H. Lee et al. 2016).

During loading, the indenter moved downward at 0.1 Å/ps (10 m/s) from an initial z position of 135 Å and reached a maximum indentation depth of 30 Å (z = 105 Å) after 300,000 timesteps (300 ps). The indenter was then held at z = 105 Å for 300,000 timesteps (300 ps). During unloading, it was withdrawn at 0.05 Å/ps (5 m/s) for 600,000 timesteps (600 ps). Thermodynamic quantities were recorded every 1,000 timesteps.

The indenter radius, maximum indentation depth, and loading and unloading speeds were selected with reference to comparable atomistic nanoindentation studies of HEA systems (Alabd Alhafez et al. 2019; D.-H. Lee et al. 2016; Liu et al. 2023). The indenter radius is large relative to the interatomic spacing, while the selected depth and loading rates remain computationally tractable for nanosecond-scale MD simulations.

3. Results and Discussion

The total energy, defined as the sum of potential and kinetic energies, was plotted as a function of temperature (Figure 1). A distinct change in the energy–temperature relation occurs near the solid-to-liquid transition. Based on this discontinuity, the melting point was estimated as:

Tm ≈ 1547 K

The structural change associated with melting was examined by comparing atomic configurations before and after the transition (Figure 2). The post-transition configuration is visibly more disordered than the initial crystalline state. Because the melting point is identified primarily from the discontinuity in the energy–temperature curve, the value should be regarded as a simulation-based estimate. The specific heat capacity at constant volume, C_v, was calculated from the energy–temperature slope according to:

$$C_v = \frac{1}{N}\left[\frac{\partial(\text{total energy})}{\partial T}\right]_V$$

where N is the total number of atoms and the derivative is evaluated from the linear fit to Figure 1. The fitted energy–temperature slope is $\delta(\text{total energy})/\delta T$

N=32000 and $\frac{\partial(\text{total energy})}{\partial T} = 8.459\ eV/K$

Thus, $C_v = \frac{1}{32000} \text{x } 8.459\ eV/atom.K$

$\Rightarrow C_v = 2.64 \text{ x } 10^{-4}\ eV/atom.K$

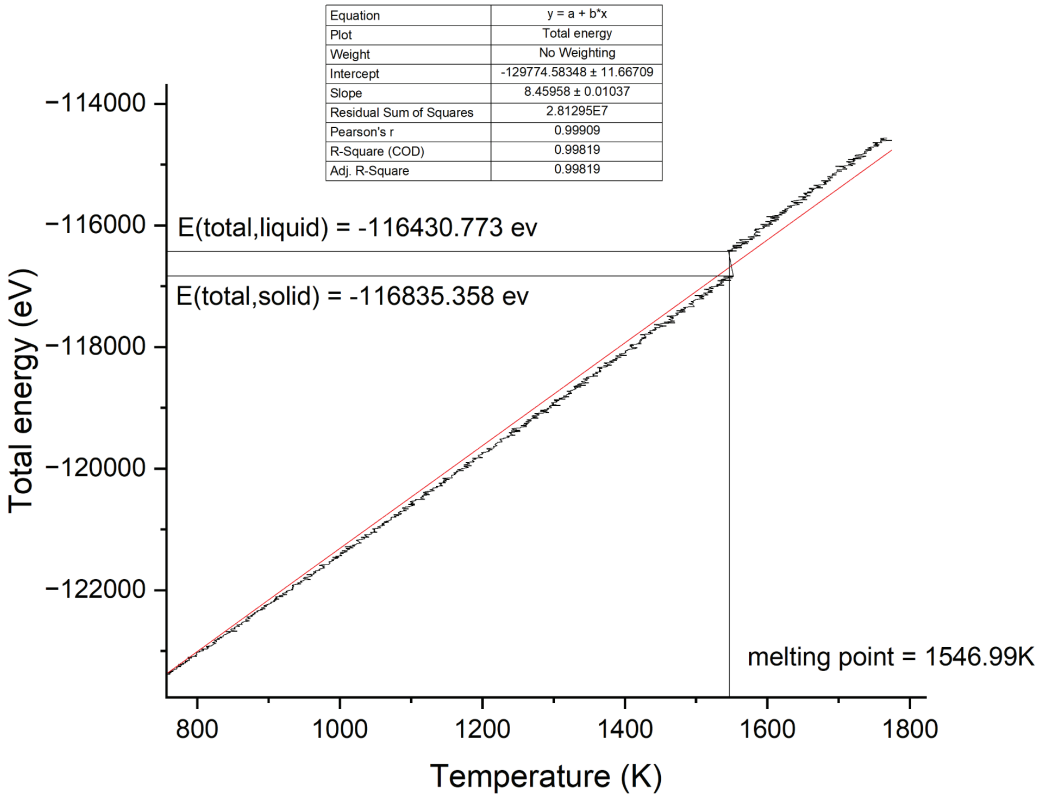


Fig. 1. Total energy as a function of temperature for the simulated Cantor alloy system.

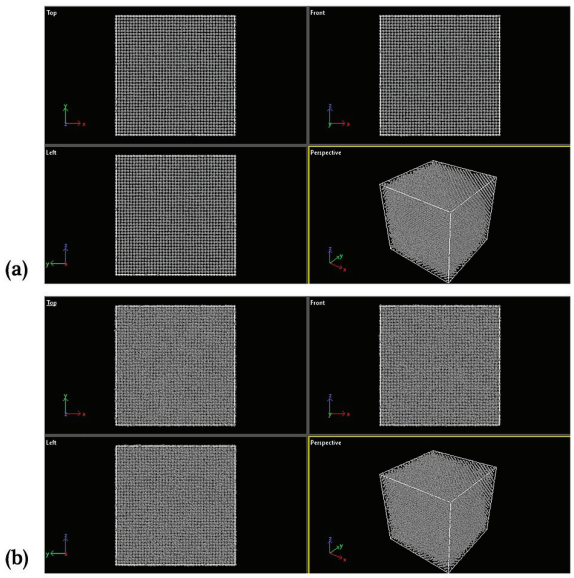


Fig. 2. Simulated Cantor alloy atomic arrangement (a) before melting and (b) immediately after melting.

To convert the result to J/(kg·K), the average molar mass of the equiatomic alloy was taken as M = 56.08 g/mol, obtained from Co (58.93 g/mol), Ni (58.69 g/mol), Cr (51.99 g/mol), Fe (55.85 g/mol), and Mn (54.94 g/mol). Using 1 eV = 1.602×10^{-19} J and $N_A = 6.022 \times 10^{23}$ atoms/mol:

$$_v = 2.64 \times 10^{-4}\ eV/(atom.K)$$

$$= (2.64 \times 10^{-4})(1.602 \times 10^{-19})\ J/(atom.K)$$

$$= 4.229 \times 10^{-23}\ J/(atom.K)$$

$$= 4.229 \times 10^{-23} \times \frac{N_A}{M}\ J/kgK$$

$$= 4.229 \times 10^{-23} \times \frac{6.022 \times 10^{23}}{56.08 \times 10^{-3}}\ J/kgK$$

$$C_v = 454.15\ J/(kg{\cdot}K)$$

The heat of fusion, ΔHf, was estimated from the discontinuous change in total energy at the melting point:

$$\Delta H_f = \frac{E_{total,liquid} - E_{total,solid}}{N}$$

From Figure 1, E(total, liquid) = −116430.773 eV and E(total, solid) = −116835.358 eV. Thus,

$$\Delta H_f = \frac{(-116430.773) - (-116835.358)}{32000} eV/atom = 0.0126\ eV/atom$$

Converting to kJ/kg:

$$\Delta H_f = 0.0126\ eV/atom$$

$$= 0.0126 \times (1.602 \times 10^{-19}) \times 10^{-3}\ kJ/atom$$

$$= 2.018 \times 10^{-24} \times \frac{N_A}{M}\ J/kg$$

$$= 2.018 \times 10^{-24} \times \frac{6.022 \times 10^{23}}{56.08 \times 10^{-3}}\ J/kg$$

$$\Delta H_f = 21.75 \frac{kJ}{kg}$$

The calculated C_v value (454 J/(kg·K)) lies at the lower end of the 450–680 J/(kg·K) range cited for Fe, Co, and Ni, whereas the calculated heat of fusion (21.75 kJ/kg) is substantially below the cited 200–300 kJ/kg range. No directly comparable experimental C_v or H_f values for the Cantor alloy under the same conditions were identified in the literature used in this study. These thermophysical values should therefore be treated as model-dependent estimates rather than as fully validated material constants. The calculated melting point, however, is consistent with previously reported values.

The effective heating rate was approximately 0.118 K/ps, obtained from the applied energy input of 1 eV/ps and the solid-state slope of the total-energy–temperature curve (8.46 eV/K; Figure 1). The calculated melting point falls within the previously reported range of 1500–1600 K (Cantor et al. 2004; Liu et al. 2023; Balyakin and Rempel 2022), indicating that no obvious excessive superheating is apparent from the resulting transition temperature.

Nanoindentation results were analysed as described in Section 2.2. Hardness and Young's modulus were calculated using the Oliver–Pharr approach (Oliver and Pharr 2004). The simulation timestep was first converted to indenter displacement for the loading and unloading stages.

(for loading phase)

disp.=(Step - Initial Step Value) * 0.0001 Å

(for unloading phase)

disp.=(Step * 0.00005) + *abs* | *Last Step Value* | Å

After conversion to displacement, the loading, holding, and unloading branches were plotted together as a load–displacement curve (Figure 3). The unloading stiffness, S, was obtained from the slope of the initial unloading segment.

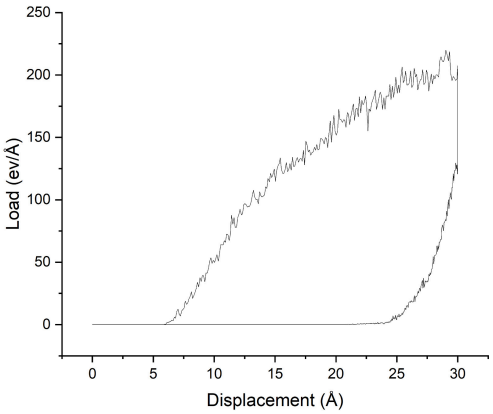


Fig. 3. Load–displacement curve from the simulated nanoindentation of the Cantor alloy.

$$S = \frac{\Delta(load)}{\Delta(displacement)} = \frac{y_2 - y_1}{x_2 - x_1}$$

From the unloading curve:

y_2 = 129.569 eV/Å = (129.569 x(1.602 x 10^{-9}))N=207.569 × 10^{-9} N

at x_2 = 29.836 Å = 29.836 × 10^{-10} m

y_1 = 86.95 eV/Å = (86.95 x(1.602 x 10^{-9}))N= 139.3 × 10^{-9} N

at x_1 = 29.136 Å = 29.136 × 10^{-10} m

Hence, $S = \frac{(207.569 - 139.3)x10^{-9}}{(29.836 - 29.136)x10^{-10}} N/m = 975.3\ N/m$

The contact depth is calculated from:

$$h_c = h_{max} - \varepsilon \frac{P_{max}}{S}$$

where h_{max} is the maximum indentation depth, P_{max} is the maximum load, and ε is a geometry-dependent constant. At the transition from holding to unloading in Figure 3, (h_{max}, P_{max}) = (29.836 Å, 129.569 eV/Å). Thus,

h_{max} = 29.836 × 10^{-10} m

P_{max} = 129.569 × (1.602 × 10^{-9}) N

P_{max} = 207.569 × 10^{-9} N

For a spherical indenter, ε = 0.75. Hence,

$$h_c = h_{max} - \varepsilon \frac{P_{max}}{S}$$

$$h_c = (29.836 \times 10^{-10}) - 0.75 \times (\frac{207.569 \times 10^{-9}}{975.3})$$

$$h_c = 28.24 \times 10^{-10}\ m$$

Using r = 29.58 × 10^{-10} m (Figure 4c), the contact area is calculated as:

$$A = f(h_c) = 2\pi r(h_c) - \pi(h_c)^2$$

$$= 2 \times \frac{22}{7} \times (29.58 \times 10^{-10}) \times (28.24 \times 10^{-10}) - \frac{22}{7} \times (28.24 \times 10^{-10})^2$$

$$= 2.74 \times 10^{-17}\ m^2$$

The hardness is calculated as:

$$H = \frac{P_{max}}{A} = \frac{207.569x10^{-9}}{2.74x10^{-17}}$$

$$H = 7.576x10^{9}\ Pa = 7.58GPa$$

The effective elastic modulus is first obtained from:

$$E_{eff} = \frac{S}{\frac{2}{\sqrt{\pi}}\sqrt{A}} = \frac{975.3}{\frac{2}{\sqrt{\pi}}\sqrt{2.74x10^{-17}}}$$

E_{eff} = 165.2 × 10^9 N/m^2 = 165.2 GPa

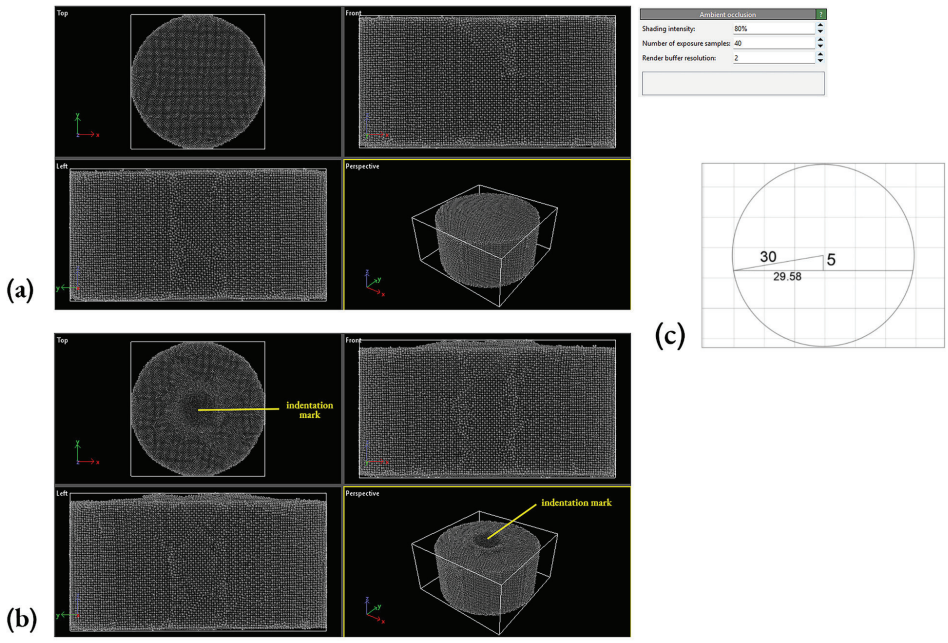


Fig. 4. Cantor alloy model (a) before loading, (b) after unloading, and (c) spherical-indenter geometry at maximum indentation. Dimensions in panel (c) are in Å.

Young's modulus is then calculated from: $\frac{1}{E_{eff}} = \frac{1-\nu^2}{E} + \frac{1-\nu_i^2}{E_i}$

where Poisson's ratio(ν)=0.32; and E_i=1140 GPa and ν_i=0.07 are Young's modulus and Poisson's ratio respectively for diamond indenter. Thus,

$$\frac{1}{165.2} = \frac{1-0.32^2}{E} + \frac{1-0.07^2}{1140}$$

$$Young's\ Modulus\ (E) = 173.3 GPa$$

The calculated Young's modulus of 173.3 GPa lies within the reported range of 160–210 GPa (Alabd Alhafez et al. 2019; Campari and Casagrande 2023; Ze Wang et al. 2020). The calculated hardness is 7.58 GPa, substantially above the 2–3 GPa values reported experimentally (Keil et al. 2021; Gianelle et al. 2022; Gludovatz et al. 2014).

The simulated indenter radius (30 Å) is much smaller and the loading rate (0.1 Å/ps ≈ 10 m/s) much higher than in typical experimental nanoindentation. In addition, the simulated crystal is defect-free and single-crystalline, whereas experimental specimens contain grain boundaries and pre-existing dislocations that facilitate plastic yielding. The assumed indenter radius and contact-area model in the Oliver–Pharr analysis also affect the absolute hardness value. The calculated hardness should therefore be interpreted as an idealized, defect-free, high-strain-rate upper-bound estimate rather than as a direct prediction of bulk polycrystalline hardness.

Table 1. Properties of the Cantor alloy calculated in this study and corresponding literature values

Property	Calculated Value	Experimental literature	Simulation literature
Melting Point	1547 K	-	1500–1600 K
Specific Heat Capacity	454 J/kg·K	-	-
Heat of Fusion	21.75 kJ/kg	-	-
Hardness	7.58 GPa	2-3 GPa	2-3 GPa
Young's Modulus	173.3 GPa	~200 GPa	160–210 GPa

4. Conclusion

This study used LAMMPS with a 2NN MEAM potential to calculate the melting point, specific heat capacity at constant volume, heat of fusion, hardness, and Young's modulus of the Cantor alloy.

(1) The calculated melting point is 1547 K, the specific heat capacity at constant volume is 454 J/(kg·K), and the heat of fusion is 21.75 kJ/kg. The melting point is consistent with reported values, whereas the calculated thermophysical quantities should be regarded as model-dependent estimates.

(2) Simulated nanoindentation gives a hardness of 7.58 GPa and a Young's modulus of 173.3 GPa. The modulus agrees with the literature range, while the hardness is higher than experimental values and is interpreted as an idealized upper-bound estimate for the defect-free, high-strain-rate model.

Overall, the results provide a consistent atomistic estimate of several thermophysical and mechanical properties of the Cantor alloy within the selected 2NN MEAM model. Experimental validation remains necessary before drawing application-level conclusions. Future work may also examine how changes in composition affect the calculated properties (T. Zhang et al. 2019).

5. Acknowledgements

This work was performed as part of the authors' Bachelor's Thesis Project (BTP), defended in May 2025 at the Department of Metallurgical and Materials Engineering, National Institute of Technology Durgapur.

The authors sincerely thank Dr. Madan Mohan Ghosh and the entire department for providing access to the Computational Laboratory for carrying out the simulations.

6. Author contributions

Rajdeep Saha contributed to software development and writing of the original draft and review. Sudipta Chell contributed to investigation, proofreading, and manuscript review. Data curation, analysis, methodology, and validation were performed jointly by both authors.

7. Data and code availability

The modified embedded-atom method (MEAM) potential files for the Cr-Co-Fe-Mn-Ni system were obtained from the NIST Interatomic Potentials Repository.

Table 2. Important parameters used in the melting-point and nanoindentation simulations

Parameter	Melting Point simulation	Nanoindentation simulation
Supercell size	20 x 20 x 20 unit cells	Cylindrical (radius & height 100 Å)
Lattice type / constant	FCC / a = 3.6 Å	FCC / a = 3.6 Å
Composition	Co Ni Cr Fe Mn equiatomic; sequential seeds – 59309, 32562, 75384, 97301, 65384	Co Ni Cr Fe Mn equiatomic; sequential seeds – 59309, 32562, 75384, 97301, 65384
Boundary conditions	Periodic (p p p)	Periodic in x y; shrink-wrapped in z (p p s)
Initial velocity	300 K, Gaussian distribution, seed 873847	300 K, Gaussian distribution, seed 873847
Equilibration ensemble / time	NVT, 300 K, 100,000 steps (100 ps), damping 0.01 ps	NVT, 300 K, 100,000 steps (100 ps), damping 0.01 ps
Timestep	1 fs (0.001 ps)	1 fs (0.001 ps)
Production ensemble	NVE with fix heat (1 eV/ps every 100 steps)	NVE with rigid spherical indenter (R = 30 Å)
Production run length	Up to 1,000,000,000 steps (1,000,000 ps) ceiling	Loading: 300,000 steps (300 ps); Holding: 300,000 steps (300 ps); Unloading: 600,000 steps (600 ps)
Indenter velocity	-	Loading: 0.1 Å/ps (10 m/s); Unloading: 0.05 Å/ps (5 m/s)
Averaging / output interval	Thermo every 10,000 steps; CFG dump every 100,000 steps	Thermo every 1,000 steps; CFG dump every 10,000 steps

The complete LAMMPS input scripts for both simulation types are available from the authors upon request.

8. Statements and Declarations

Competing interests: The authors declare no competing financial or non-financial interests.

9. References

Alabd Alhafez, Iyad, Carlos J. Ruestes, Eduardo M. Bringa, and Herbert M. Urbassek. 2019. "Nanoindentation into a High-Entropy Alloy – An Atomistic Study." Journal of Alloys and Compounds 803 (September): 618–24. https://doi.org/10.1016/j.jallcom.2019.06.277

Balyakin, Ilya, and Andrey Rempel. 2022. "Atomistic Calculation of the Melting Point of the High-Entropy Cantor Alloy CoCrFeMnNi." Doklady Physical Chemistry 502 (April): 11–17. https://doi.org/10.1134/S0012501622010018

Campari, Enrico Gianfranco, and Angelo Casagrande. 2023. "Mechanical Spectroscopy Study of CrNiCoFeMn High-Entropy Alloys." Materials 16 (10): 3689. https://doi.org/10.3390/ma16103689

Cantor, B., I. T. H. Chang, P. Knight, and A. J. B. Vincent. 2004. "Microstructural Development in Equiatomic Multicomponent Alloys." Materials Science and Engineering: A 375–377 (July): 213–18. https://doi.org/10.1016/j.msea.2003.10.257

Caramarin, Stefania, Ioana-Cristina Badea, Laurentiu-Florin Mosinoiu, et al. 2024. "Structural Particularities, Prediction, and Synthesis Methods in High-Entropy Alloys." Applied Sciences 14 (17): 17. https://doi.org/10.3390/app14177576

Choi, Won-Mi, Yong Hee Jo, Seok Su Sohn, Sunghak Lee, and Byeong-Joo Lee. 2018. "Understanding the Physical Metallurgy of the CoCrFeMnNi High-Entropy Alloy: An Atomistic Simulation Study." Npj Computational Materials 4 (1): 1. https://doi.org/10.1038/s41524-017-0060-9

Gali, A., and E. P. George. 2013. "Tensile Properties of High- and Medium-Entropy Alloys." Intermetallics 39 (August): 74–78. https://doi.org/10.1016/j.intermet.2013.03.018

Gianelle, Madison A., Chase Clapp, Animesh Kundu, and Helen M. Chan. 2022. "Solid State Processing of the Cantor Derived Alloy CoCrFeMnNi by Oxide Reduction." Results in Materials 14 (June): 100286. https://doi.org/10.1016/j.rinma.2022.100286

Gludovatz, Bernd, Anton Hohenwarter, Dhiraj Catoor, Edwin H. Chang, Easo P. George, and Robert O. Ritchie. 2014. "A Fracture-Resistant High-Entropy Alloy for Cryogenic Applications." Science (New York, N.Y.) 345 (6201): 1153–58. https://doi.org/10.1126/science.1254581

Gong, Zheyu, Lixian Yang, Yong Cao, Junfeng Liu, and Shenggang Zhou. 2025. "The Influence of Mn Content, Temperature, and Strain Rate on the Mechanical Behavior of FeNiCrCoMn High-Entropy Alloys under Tensile and Compressive Loads: A Molecular Dynamics Simulation Study." Materials Today Communications 46 (June): 112532. https://doi.org/10.1016/j.mtcomm.2025.112532

Jin, Z. H., P. Gumbsch, K. Lu, and E. Ma. 2001. "Melting Mechanisms at the Limit of Superheating." Physical Review Letters 87 (5): 055703. https://doi.org/10.1103/PhysRevLett.87.055703

Kauffmann, Alexander, Michael Stüber, Harald Leiste, et al. 2017. "Combinatorial Exploration of the High Entropy Alloy System Co-Cr-Fe-Mn-Ni." Surface and Coatings Technology 325 (September): 174–80. https://doi.org/10.1016/j.surfcoat.2017.06.041

Keil, Tom, Daniel Utt, Enrico Bruder, Alexander Stukowski, Karsten Albe, and Karsten Durst. 2021. "Solid Solution Hardening in CrMnFeCoNi-Based High Entropy Alloy Systems Studied by a Combinatorial Approach." Journal of Materials Research 36 (12): 2558–70. https://doi.org/10.1557/s43578-021-00205-6

Kim, Young-Kyun, Sangsun Yang, and Kee-Ahn Lee. 2020. "Superior Temperature-Dependent Mechanical Properties and Deformation Behavior of Equiatomic CoCrFeMnNi High-Entropy Alloy Additively Manufactured by Selective Laser Melting." Scientific Reports 10 (1): 8045. https://doi.org/10.1038/s41598-020-65073-2

Lee, Byeong-Joo, M. I. Baskes, Hanchul Kim, and Yang Cho. 2001. "Second Nearest-Neighbor Modified Embedded Atom Method Potentials for Bcc Transition Metals." Physical Review B 64 (October). https://doi.org/10.1103/PhysRevB.64.184102

Lee, Byeong-Joo, Won-Seok Ko, Hyun-Kyu Kim, and Eun-Ha Kim. 2010. "The Modified Embedded-Atom Method Interatomic Potentials and Recent Progress in Atomistic Simulations." Calphad 34 (4): 510–22. https://doi.org/10.1016/j.calphad.2010.10.007

Lee, Dong-Hyun, Moo-Young Seok, Yakai Zhao, et al. 2016. "Spherical Nanoindentation Creep Behavior of Nanocrystalline and Coarse-Grained CoCrFeMnNi High-Entropy Alloys." Acta Materialia 109 (May): 314–22. https://doi.org/10.1016/j.actamat.2016.02.049

Liu, Y. Z., J. Sun, H. L. Li, et al. 2023. "Molecular Dynamics Simulations for Nanoindentation Response of Metastable High Entropy Alloy." Journal of Materials Research 38 (10): 2838–51. https://doi.org/10.1557/s43578-023-01011-y

Lohmuller, Paul, Laurent Peltier, Alain Hazotte, Julien Zollinger, Pascal Laheurte, and Eric Fleury. 2018. "Variations of the Elastic Properties of the CoCrFeMnNi High Entropy Alloy Deformed by Groove Cold Rolling." Materials 11 (8): 1337. https://doi.org/10.3390/ma11081337

Mahata, Avik, Tanmoy Mukhopadhyay, and Mohsen Asle Zaeem. 2022. "Modified Embedded-Atom Method Interatomic Potentials for Al-Cu, Al-Fe and Al-Ni Binary Alloys: From Room Temperature to Melting Point." Computational Materials Science 201 (January): 110902. https://doi.org/10.1016/j.commatsci.2021.110902

Maier-Kiener, Verena, Benjamin Schuh, Easo P. George, Helmut Clemens, and Anton Hohenwarter. 2017. "Insights into the Deformation Behavior of the CrMnFeCoNi High-Entropy Alloy Revealed by Elevated Temperature Nanoindentation." Journal of Materials Research 32 (14): 2658–67. https://doi.org/10.1557/jmr.2017.260

Oliver, W. C., and G. M. Pharr. 2004. "Measurement of Hardness and Elastic Modulus by Instrumented Indentation: Advances in Understanding and Refinements to Methodology." Journal of Materials Research 19 (1): 3–20. https://doi.org/10.1557/jmr.2004.19.1.3

Otto, F., A. Dlouhý, Ch. Somsen, H. Bei, G. Eggeler, and E. P. George. 2013. "The Influences of Temperature and Microstructure on the Tensile Properties of a CoCrFeMnNi High-Entropy Alloy." Acta Materialia 61 (15): 5743–55. https://doi.org/10.1016/j.actamat.2013.06.018

Özgün, Özge, David Koch, Asli Cakir, et al. 2022. "Magnetic Properties of Fcc and σ Phases in Equiatomic and Off-Equiatomic High-Entropy Cantor Alloys." Physical Review B 106 (December). https://doi.org/10.1103/PhysRevB.106.214422

Pei, Zongrui, Shiteng Zhao, Martin Detrois, et al. 2023. "Theory-Guided Design of High-Entropy Alloys with Enhanced Strength-Ductility Synergy." Nature Communications 14 (1): 2519. https://doi.org/10.1038/s41467-023-38111-6

Sun, S. J., Y. Z. Tian, X. H. An, H. R. Lin, J. W. Wang, and Z. F. Zhang. 2018. "Ultrahigh Cryogenic Strength and Exceptional Ductility in Ultrafine-Grained CoCrFeMnNi High-Entropy Alloy with Fully Recrystallized Structure." Materials Today Nano 4 (December): 46–53. https://doi.org/10.1016/j.mtnano.2018.12.002

Thompson, Aidan P., H. Metin Aktulga, Richard Berger, et al. 2022. "LAMMPS - a Flexible Simulation Tool for Particle-Based Materials Modeling at the Atomic, Meso, and Continuum Scales." Computer Physics Communications 271 (February): 108171. https://doi.org/10.1016/j.cpc.2021.108171

Wang, Ze, Cheng Wang, Yi-Lu Zhao, et al. 2020. "Growth, Microstructure and Mechanical Properties of CoCrFeMnNi High Entropy Alloy Films." Vacuum 179 (September): 109553. https://doi.org/10.1016/j.vacuum.2020.109553

Wang, Zhangwei, Wenjun Lu, Dierk Raabe, and Zhiming Li. 2019. "On the Mechanism of Extraordinary Strain Hardening in an Interstitial High-Entropy Alloy under Cryogenic Conditions." Journal of Alloys and Compounds 781 (April): 734–43. https://doi.org/10.1016/j.jallcom.2018.12.061

Wei, Daixiu, Wu Gong, Tomohito Tsuru, et al. 2022. "Mechanical Behaviors of Equiatomic and Near-Equiatomic Face-Centered-Cubic Phase High-Entropy Alloys Probed Using in Situ Neutron Diffraction." International Journal of Plasticity 158 (November): 103417. https://doi.org/10.1016/j.ijplas.2022.103417

Yeh, Jien-Wei, S. K. Chen, Su-Jien Lin, et al. 2004. "Nanostructured High□Entropy Alloys with Multiple Principal Elements: Novel Alloy Design Concepts and Outcomes." Advanced Engineering Materials 6 (May): 299–303. https://doi.org/10.1002/adem.200300567

Yue, Yuanying, Xuehui Yan, and Yong Zhang. 2022. "Nano-Fiber-Structured Cantor Alloy Films Prepared by Sputtering." Journal of Materials Research and Technology 21 (November): 1120–27. https://doi.org/10.1016/j.jmrt.2022.09.107

Zeng, Zhihua, Mengqi Xiang, Dan Zhang, et al. 2021. "Mechanical Properties of Cantor Alloys Driven by Additional Elements: A Review." Journal of Materials Research and Technology 15 (November): 1920–34. https://doi.org/10.1016/j.jmrt.2021.09.019

Zhang, Liang, Kun Qian, Jun Huang, Mao Liu, and Yasushi Shibuta. 2021. "Molecular Dynamics Simulation and Machine Learning of Mechanical Response in Non-Equiatomic FeCrNiCoMn High-Entropy Alloy." Journal of Materials Research and Technology 13 (July): 2043–54. https://doi.org/10.1016/j.jmrt.2021.06.021

Zhang, Tao, Lijun Xin, Fufa Wu, et al. 2019. "Microstructure and Mechanical Properties of FexCoCrNiMn High-Entropy Alloys." Journal of Materials Science & Technology 35 (10): 2331–35. https://doi.org/10.1016/j.jmst.2019.05.050